DOI:10.26599/FSHW.2026.9251190

Contents lists available at SciOpen

Food Science and Human Wellness

journal homepage: https://www.sciopen.com/journal/2097-0765

China Food Publishing Co.

Structural characterization of *Auricularia heimuer* polysaccharide and its protection against drug-induced liver injury via AMPK/GSK3β, Nrf2/HO-1 signaling and gut microbiota modulation

Yingdi Dai[a,b], Detian Li[a,b], Sijia Ma[a,b], Yuan Sun[a,b], Hongxiang Liu[a,b], Miao Ding[a,b], Qi Wang[a,b,*], Yang Liu[a,b,*]

[a] *Engineering Research Center of Chinese Ministry of Education for Edible and Medicinal Fungi, Jilin Agricultural University, Changchun 130118, China*

[b] *College of Plant Protection, College of Mycology, Jilin Agricultural University, Changchun 130118, China*

ABSTRACT: Excessive use of acetaminophen (APAP) significantly contributes to drug-induced liver injury (DILI). *Auricularia heimuer* polysaccharides have significant hepatoprotective potential, however their mode of action in mitigating DILI is not yet elucidated. This study isolated and purified a novel polysaccharide, Ahp-1, from the fruiting bodies of *A. heimuer*, with a molecular weight of 270.161 kDa. Structural analysis revealed that the principal glycosidic linkages in Ahp-1 are 6-Gal, 6-Glc, t-Fuc, and 2,6-Gal, which form dimers by cross-linking of polysaccharide chains. Animal studies indicated that Ahp-1 reduces oxidative stress, elevates the relative abundance of beneficial bacteria within the gut microbiota, regulates microbial balance, and promotes the synthesis of favorable metabolites like Trigonelline. Moreover, following fecal microbiota transplantation (FMT), Ahp-FMT augments tight junction proteins and short-chain fatty acids (SCFAs), thus restoring the intestinal barrier. This subsequently stimulates the AMPK/GSK3β and Nrf2/HO-1 signaling pathways to mitigate DILI. These results provide novel opportunities for using *A. heimuer* polysaccharides as functional foods or hepatoprotective agents.

Keywords: *Auricularia heimuer* polysaccharide, Oxidative damage, Gut microbiota, Drug-induced liver injury

1. Introduction

Acetaminophen (APAP) is a commonly used antipyretic and analgesic in clinical environments. Demonstrates significant therapeutic efficacy at appropriate doses[1-2]. Nonetheless, an overdose of APAP may lead to sudden liver failure. At therapeutic quantities, APAP is excreted via glutathione (GSH). Excessive alcohol consumption depletes GSH, leading to oxidative stress[3]. This would disrupt the microbial balance and increase the accumulation of toxic metabolites[4-5]. Furthermore, APAP overdose may disrupt tight junction proteins, leading to reduced concentrations of short-chain fatty acids (SCFAs)[6]. N-acetylcysteine (NAC), used as an antidote for acetaminophen-induced liver damage, has a limited therapeutic range and is associated with specific severe side effects[7]. Thus, the discovery of novel therapeutic compounds that combine high efficacy and safety offers a new strategy for the early prevention of APAP-induced liver injury.

Auricularia heimuer is a member of the Auriculariaceae family of the genus *Auricularia*, characterized

***Corresponding author**
qiwang@jlau.edu.cn. y_liu10@jlau.edu.cn.

Received 14 October 2025
Received in revised from 22 November 2025
Accepted 11 February 2026

by significant nutritional and therapeutic properties[8]. Polysaccharides, being the principal active constituents, exhibit pharmacological features such as antioxidant[9], antitumour[10], and immunomodulatory actions[11]. According to literature reports, *A. heimuer* polysaccharides exhibit significant hepatoprotective potential, alleviating immune-mediated liver injury by regulating bile acid and arachidonic acid metabolism via the gut microbiota[12]. Moreover, it can inhibit the TLR4/NF-κB pathway, activate the Nrf2/HO-1 pathway, suppress the activation of quiescent hepatic stellate cells (HSCs) and extracellular matrix (ECM) deposition, thereby alleviating CCl_4-induced chemical liver injury[13]. However, the mechanism by which *A. heimuer* polysaccharides alleviate drug-induced liver injury (DILI) remains ambiguous.

This study isolated and purified a novel polysaccharide fraction, Ahp-1, from the fruiting bodies of *A. heimuer* via column chromatography. The structure was analyzed using methylation analysis, atomic force microscopy (AFM), and scanning electron microscopy (SEM). Additionally, the protective role of Ahp-1 against APAP-induced DILI was examined using fecal microbiota transplantation (FMT), 16S rRNA sequencing, non-targeted metabolomics, and western blot analysis. This study elucidates the structure of Ahp-1 and its mechanism of action in ameliorating DILI, proposing an innovative therapeutic approach for DILI. It establishes the experimental foundation for advancing the application of *A. heimuer* polysaccharides as a potential hepatoprotective agent.

2. Materials and methods

2.1 Extraction and purification of Ahp-1

The fruiting bodies of *A. heimuer* (cultivated in Zhashui County, Shangluo City, Shaanxi Province, China) were ground and sifted through a 60-mesh sieve. Distilled water was included at 1:30, extracted for 3 h, and the supernatant was then concentrated. After precipitation and deproteinization, the extract was purified via DEAE-52 cellulose anion exchange chromatography (Column material: Beijing Solepol Science and Technology Co., Ltd., Beijing, China, Columns: Shanghai Lianta Instruments, 4 cm × 50 cm, Shanghai, China), yielding three fractions: Ah-1, Ah-2, and Ah-3. The obtained Ah-1 fraction was applied to a Sephacryl S-400 HR column (Cytiva, Cat# 17060901, Shanghai, China), eluted with ultrapure water, collected, dialyzed for concentration, freeze-dried, and analyzed for polysaccharide content using phenol-sulfuric acid (Beijing Chemical Factory, Beijing, China).

2.2 Structural characterization of Ahp-1

2.2.1 Molecular weight distribution

In gel permeation chromatography (GPC), the porous gel in the columns segregates polysaccharide components according to variations in molecular size. The eluent then passes through a refractive index (RI) detector and a multi-angle laser light scattering (MALS) detector in succession. The concentrations of each polysaccharide component are accurately calculated by comparing the refractive index changes between the sample and the mobile phase. By using laser scattering signals at various angles and integrating the

concentrations obtained by RI, the molecular weight of each component is directly determined, thoroughly representing the molecular structural attributes of the polysaccharides[14].

2.2.2 Infrared spectral analysis

Chromatographic-grade KBr 200 mg (Beijing Chemical Plant, Beijing, China) and 2 mg of Ahp-1[15]. The blend was meticulously combined in a dry environment, pulverized, crushed into tablets, and examined using a Nicolet™ iS5 infrared spectrometer (Thermo Fisher Scientific, Massachusetts, USA).

2.2.3 Ultraviolet-Visible (UV) spectral analysis

The UV spectrum of the Ahp-1 solution was obtained using a UV spectrophotometer (Analytik Jena, Spectroc 200 plus, Germany) throughout the wavelength spectrum of 200-400 nm.

2.2.4 Monosaccharide composition analysis

Accurately measure 5 mg of the Ahp-1 sample into a sterile chromatographic vial. Subsequently, 1 mL of 2 M TFA solution (Beijing Chemical Factory, Beijing, China) was included and subjected to heating at 121 ℃ for 2 h. Nitrogen was introduced into the mixture and subsequently evaporated to dryness. The samples were washed with 99.99% methanol (Beijing Chemical Factory, Beijing, China), evaporated to dryness. The samples were thereafter dissolved in sterile water and transported to chromatography vials for analysis. An ICS5000 ion chromatography system (Thermo Fisher Scientific, Massachusetts, USA) equipped with an electrochemical detector was used to evaluate and identify monosaccharide constituents[16].

2.2.5 Methylation analysis

Weigh 3 mg of Ahp-1 sample, dissolve, then add 1 mg NaOH (Sinopharm Chemical Reagent Co., Ltd., Shanghai, China) and incubate for 30 min. Following incubation, add 50 μL of methyl iodide solution (Tianjin Xintong Fine Chemical Co., Ltd., Tianjin, China) and react for 1 h. Then add 1 mL water and 2 mL dichloromethane (Tianjin Xintong Fine Chemical Co., Ltd., Tianjin, China), mix thoroughly, centrifuge, and discard the aqueous phase. Repeat this procedure three times. Add 100 μL 2 mol/L TFA (Sigma-Aldrich, Shanghai, China), react at 121 ℃ for 90 min, then evaporate to dryness at 30 ℃. Add 50 μL 2 mol/L ammonia solution and 50 μL 1 mol/L $NaBD_4$ (Beijing Chemical Factory, Beijing, China), mix thoroughly, and react at room temperature for 2.5 h. Add 20 μL acetic acid (Beijing Chemical Factory, Beijing, China) to terminate the reaction. Evaporate to dryness under nitrogen, wash twice with 250 μL methanol (ANPEL Shanghai, China), and evaporate to dryness again under nitrogen. Add 250 μL acetic anhydride, vortex to mix, and react for 2.5 h. Finally, add 1 mL water and allow to stand for 10 min. Add 500 μL dichloromethane, centrifuge, discard the aqueous layer, and repeat the washing procedure three times. Collect the lower dichloromethane layer for GC-MS analysis. Analysis was performed using an Agilent gas chromatography system (Agilent Technologies, Agilent 7890A, California, USA) coupled with an Agilent quadrupole mass spectrometry detector (Agilent Technologies, Agilent 5977B, California, USA).

2.3 Crystallographic characteristics and surface molecular morphology of Ahp-1

2.3.1 AFM analysis

After ultrasonic cleaning and air-drying, the Ahp-1 sample was affixed to a mica substrate for examination using an atomic force microscope (Furui Precision Instruments Co., Ltd., Shanghai, China). The atomic force microscope was preheated for 30 min before use. A silicon probe was used, with the following settings: tapping mode (amplitude 5-30 nm), scanning range 1-100 μm, scanning rate 0.5-2 Hz, and resolution 512 × 512 pixels.

2.3.2 Raman spectroscopy analysis

The Ahp-1 sample was fixed after undergoing a drying procedure. The DXR3 Flex spectrometer (Thermo Fisher Scientific, Massachusetts, USA) was activated and warmed. A 785 nm laser was used, and the optical path was calibrated. The first laser power was established at 0.1% within a spectral range of 100-4000 cm^{-1}. The spectra were obtained by scanning various places, and the results were recorded.

2.3.3 SEM analysis

The Ahp-1 sample was affixed to the stage using a conductive glue. After vacuum sputter-coating with gold (5-10 nm thickness), the stage was relocated to the sample chamber. The specimen was examined under circumstances of elevated vacuum voltage, with pictures captured at magnifications of 20, 50, and 500[17].

2.4 Animal models and animal ethics

Male KM mice classified as SPF, weighing 30-40 g, were procured from the Laboratory Animal Center at Jilin Agricultural University. All mice were raised in a specialized pathogen-free animal facility. The mice were acclimatized for one week. All research was conducted in accordance with the rules established by the Laboratory Animal Welfare and Ethics Committee of Jilin Agricultural University. This study adhered to the EU Directive 2010/63 on the protection of animals used for scientific purposes. The animal ethical approval number was 2024 08 08 001.

2.4.1 Gavage experiments with Ahp-1

The Ahp-1 experimental groups (50, 100, and 200 mg/kg) were administered the respective dosages of Ahp-1 for a duration of 20 consecutive days. The positive control (PC) group was administered 150 mg/kg NAC (Solaibao Technology Co., Ltd., Beijing, China) by oral gavage one hour before modeling. The remaining groups were administered physiological saline by oral gavage. All groups, with the exception of the CK group, were given a single oral dosage of 200 mg/kg of APAP (Beijing Solibao Technology Co., Ltd., Beijing, China) on day 21 to create a DILI model.

2.4.2 Antibiotic (ABX) pretreatment and FMT experiments

Sterile aqueous formulations of ABX were prepared. The ABX solution consisted of ampicillin 1 g/L, neomycin sulfate 1 g/L, metronidazole 1 g/L (Macklin, Shanghai, China), and vancomycin 500 mg/L (Aladdin, Guangzhou, China), used to create a quasi-sterile mouse model. Following acclimation feeding, mice were provided with sterile regular chow and sterile drinking water injected with antibiotics, which were replaced every two days. Food and drinking water were then eaten without limitation. The mice were consistently fed for one week to establish a proposed germ-free mouse model. Following model establishment, validation was conducted using DNA and 16S RNA.

Establishment of fecal donor mice: The CK group received continuous oral saline administration. The APAP group received daily oral saline administration, supplemented with a 200 mg/kg APAP solution on the final day. The medium-dose Ahp-1 group received daily gastric lavage with 100 mg/kg polysaccharide solution, supplemented with 200 mg/kg APAP solution on the final day. Fecal samples were collected at initial, intermediate, and terminal stages, with 5-6 fecal pellets obtained per animal. Intra-group mixed samples cryopreservation.

Fecal transplant group: Ten standard SPF mice constituted the CK group, receiving oral saline administration (0.2 ml per mouse). The CK group, APAP group, and polysaccharide group underwent mixed transplantation via oral administration of fecal suspension solution (0.2 ml per mouse) every other day for three weeks. On the final day, a 200 mg/kg APAP solution was administered. The fecal transplantation failure experiment followed the same dosing regimen as above, but required continuous provision of sterile drinking water containing antibiotics for 3 weeks.

2.4.3 Toxicity assessment studies

20 KM mice were divided into a CK group and an Ahp-1 group. The CK group received daily oral administration of physiological saline, while the Ahp-1 group received daily oral administration of a polysaccharide solution at 200 mg/kg for 21 consecutive days. Body weight changes were recorded throughout the period.

2.4.4 Antagonist experiment

Antagonist Dorsomorphin (Compound C) purchased from MedChemExpress, Cat# BML-275, Shanghai, China. The CK group received daily gastric lavage with physiological saline. The APAP group received daily gastric lavage with physiological saline, followed by a final gastric lavage with 200 mg/kg APAP solution on the last day. The Ahp-1+APAP+Compound C group received daily gastric lavage with polysaccharide solution, followed by a final gastric lavage with 200 mg/kg APAP solution on the last day and an injectable inhibitor. The Ahp-FMT+APAP+Compound C group received daily oral administration of fecal suspension, with a final dose of 200 mg/kg APAP solution on the last day and an injectable inhibitor.

2.5 Measurement of liver index

The body weight of the mouse was recorded, and the liver was flushed with physiological saline, weighed, and the corresponding organ index was calculated.

2.6 Histopathological analysis

The fixed liver tissue was embedded in paraffin and underwent haematoxylin and eosin (H&E) staining using haematoxylin provided by Beijing Solarbio Science & Technology Co., Ltd. Histopathological evaluation was conducted by analyzing tissue slices using an optical microscope[18].

2.7 Serum and liver biochemical analysis

The biochemical markers alanine aminotransferase (ALT) (JM-02543M2), aspartate aminotransferase (AST) (JM-03113M2), superoxide dismutase (SOD) (JM-02672M2), glutathione peroxidase (GSH-Px) (JM-03038M2), malondialdehyde (MDA) (JM-13017M2) and catalase (CAT) (JM-05056H2) were assessed using the kit from Jiangsu Jingmei Biological Technology Co., Ltd (Jiangsu, China).

2.8 Intestinal flora analysis

DNA was extracted from collected intestinal contents using a DNA extraction kit (Biyuntian Biotechnology Co., Ltd., Shanghai, China). The V3-V4 region of the bacterial 16S rRNA gene was amplified using primers 338F/806R to assess microbial community composition. DNA from caecal contents underwent paired-end sequencing on an Illumina platform (Illumina, California, USA). Sequence denoising and clustering were performed on raw sequencing data**.** High-quality sequences were clustered at 97% similarity. Operational taxonomic units **(**OTUs**)** from different units underwent species annotation[19]. Alpha and beta diversity were assessed to analyse the diversity of characterised species within the microbiota, respectively.

2.9 Non-targeted metabolomics analysis

Take 200 μL of serum, add 100 μL of 15% phosphoric acid (Sinopharm Chemical Reagents Co., Ltd., Shanghai, China), then add 375 μg/mL internal standard (4-methylpentanoic acid, Sigma-Aldrich, Shanghai, China) and 280 μL of diethyl ether (Sinopharm Chemical Reagent Co., Ltd., Shanghai, China). Homogenise for 1 min, centrifuge at 4 ℃ for 10 min, and test the supernatant. Analysis was performed using a Thermo Trace 1300 gas chromatography system (Thermo Fisher Scientific, Massachusetts, USA) coupled with an Agilent HP-INNOWAX capillary column (30 m × 0.25 mm × 0.25 μm, Agilent, California, USA). Mass spectrometry detection employed a Thermo ISQ 7000 mass spectrometer (Thermo Fisher Scientific, Massachusetts, USA) utilising an electron impact ionisation (EI) source with an electron energy of 70 eV. P-values were computed using t-tests or ANOVA for the first assessment of differential metabolites. The metabolites were assigned to KEGG pathways, accompanied by rigorous statistical analysis to identify highly enriched pathways[20].

2.10 SCFAs assay

Fecal samples stored at -80 ℃ were thawed on wet ice for SCFAs determination. Two millilitres of thawed fermentate were taken, mixed with sulphuric acid solution (Beijing Chemical Factory, Beijing, China) by shaking, and left to stand for 30 min. The mixture was then centrifuged at 4 ℃ for 20 min, The supernatant was filtered through a 0.22 μm aqueous phase filter membrane (Tianjin Jinteng Laboratory Equipment Co., Ltd., Tianjin, China), degassed, and transferred to a liquid phase vial. Chromatography was performed using an Inert Sustain AQC18 column (150 mm × 2.1 mm, GL Sciences, Tokyo, Japan) at a flow rate of 0.5 mL/min. detection wavelength 210 nm. Mobile phase A was 20 mmol/L NaH_2PO_4 (Sinopharm Chemical Reagent Co., Ltd., Shanghai, China); B was acetonitrile (Sinopharm Chemical Reagent Co., Ltd., Shanghai, China).

2.11 Immunofluorescence analysis

Colon tissue was preserved and embedded in paraffin, and sectioned using a low-temperature microtome (Oxford Instruments Technology Co., Ltd., Shanghai, China). The sections were then dewaxed in xylene (Shanghai Denuo Chemical Co., Ltd., Shanghai, China) for 30 min and dehydrated with ethanol at different concentrations. After antigen retrieval via steaming in sodium citrate buffer (Beijing Baierdi Biotechnology Co., Ltd., Beijing, China) for 30 min, incubate overnight with blocking agent and primary antibody. Subsequent to washing, the sections were incubated in darkness with the corresponding fluorescent secondary antibody. The sections were stained for a duration of 15 min. Fluorescent intestinal proteins were seen, and digital pictures were obtained using an Eclipse C1 fluorescent microscope (Nikon, Tokyo, Japan)[21].

2.12 Cell line and metabolites in vitro cell experiments

Human normal hepatocytes (THLE-2) were purchased from the Beijing BeNa Cell Bank (Beijing, China).

THLE-2 cells were seeded into 96-well plates (NEST Biotechnology, Wuxi, China). The following groups were established: CK group: No APAP, no Trigonelline, equal volume of solvent (DMSO, final concentration ≤ 0.1%). APAP group: APAP monotherapy, treated with 15 mmol/L APAP for 24 h. Trigonelline intervention group: 50 μmol/L Trigonelline pre-treatment for 2 h, followed by APAP co-incubation for 24 h. Trigonelline group: Trigonelline monotherapy, treated with 50 μmol/L Trigonelline for 24 h[22]. Subsequently, oxidative function validation was performed using SOD (ADS-W-KY011-48), CAT (ADS-W-KY002-48), MDA (ADS-W-YH002-48), and GSH-Px (ADS-F-G003-48) assay kits procured from Jiangsu Addison Biotechnology Co., Ltd..

THLE-2 cells were seeded into 96-well plates and treated for 12, 24, and 48 h respectively according to the aforementioned experimental protocol. Cell viability was subsequently determined using the Cell Counting Kit-8 (CCK-8) assay kit (APExBIO, K1018, Houston, USA).

2.13 Western blot analysis

Proteins were extracted from liver tissue using a mixture containing protease inhibitors, phosphatase inhibitors, and cell lysis buffer (Beyotime Biotechnology Co., Ltd., Shanghai, China). After centrifugation,

the supernatant was collected and protein concentration was determined using the bicinchoninic acid assay (BCA) kit (Beyotime Biotechnology, Shanghai, China). Equal volumes of protein were separated by 8-12% sodium dodecyl sulphate-polyacrylamide gel electrophoresis (SDS-PAGE) and transferred onto nitrocellulose (NC) membranes. Following blocking with fast blocking western (HYCEZMBIO, Wuhan, China), membranes were incubated overnight with primary antibodies. Analysis was performed using an enhanced chemiluminescence (ECL) kit (Meilunbio, Dalian, China), followed by visualisation with a Gene Gnome XRD automated imaging system (Syngene, Cambridge, UK). Relative protein expression was quantified and normalised using ImageJ software (NIH, Bethesda, MD, USA). Specific information about antibody use is shown in Tab. S1. Western blot analysis was performed with liver tissue samples from three independent animal experiments, and each biological replicate was conducted with three technical replicates for quality control. The quantitative data were analyzed based on the results of biological replicates.

2.13 Statistical Analysis

All experimental results are presented as mean ± standard deviation (SD). Statistical analyses were conducted using the software packages Origin (Origin Lab Inc., San Mateo, USA), ImageJ (National Institutes of Health, USA), and GraphPad Prism 8 (Graphpad Inc., San Diego, CA, USA).

3. Results and discussion

3.1 Isolation and purification of Ahp-1, molecular weight determination, and monosaccharide composition analysis

Crude polysaccharides were extracted from *A. heimuer* using hot water and then purified using DEAE-52 column chromatography, yielding polysaccharide fractions Ah-1, Ah-2, and Ah-3. Preliminary experiments revealed that Ah-1 demonstrated the most potent efficacy in ameliorating DILI (Fig. S1A-B). Consequently, we subjected Ah-1 to secondary purification using a Sephacryl S-400 HR chromatography column, yielding Ahp-1 with a polysaccharide content of 70.58% (Fig. 1A-B). Consequently, Ahp-1 was selected for further testing. Ahp-1 had a weight-average molecular weight of 270.161 kDa (Fig. 1C). UV-visible spectroscopy showed no notable absorption peaks at 260 or 280 nm, indicating exceptional sample purity and the lack of proteins or nucleic acids (Fig. 1D). The monosaccharide composition of Ahp-1 included galactose, glucose, fucose, mannose, and rhamnose, with molar ratios of 41.56%, 28.28%, 22.33%, 7.20%, and 0.64%, respectively (Fig. 1E).

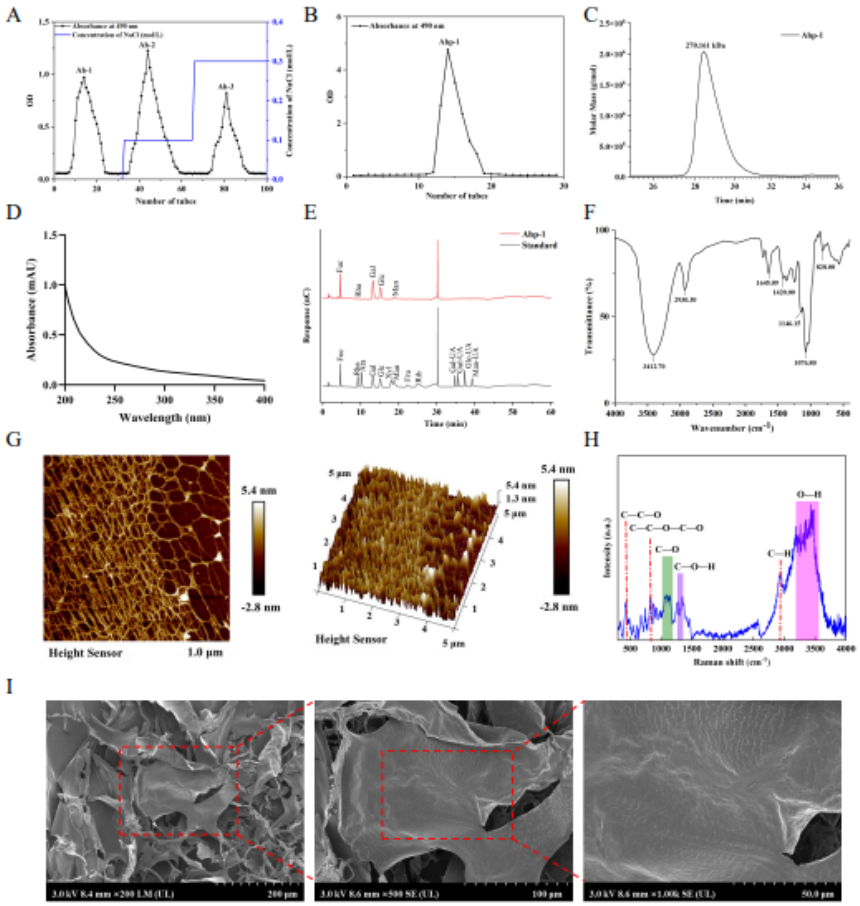

Fig. 1. Isolation, purification, and structural characterization of *Auricularia heimuer* polysaccharide (Ahp-1). (A) DEAE-52 elution curve. (B) Sephacryl S-400 elution curve. (C) Molecular weight distribution. (D) Ultraviolet-visible spectroscopy. (E) Monosaccharide composition. (F) Fourier infrared spectrogram. (G) Atomic force microscope. (H) Raman spectroscopy. (I) Scanning electron microscope.

3.2 Infrared spectral analysis

The infrared spectrum of Ahp-1 is presented in Fig. 1F. The strong absorption peak at 3412.70 cm^{-1} was attributed to the O-H stretching vibration of hydroxyl groups[23]. The peak at 2930.30 cm^{-1} corresponded to C-H stretching vibrations in the polysaccharide, specifically the asymmetric stretching of C-H in -CH groups[24]. The 1645.09 cm^{-1} peak was linked to subtle minor C=O stretching vibrations within polysaccharide molecules[25]. The 1420.00 cm^{-1} peak was related to C-H or -OH bending vibrations[26]. The absorption at 1146.15 cm^{-1} was assigned to the asymmetric stretching of C-O-C glycosidic bonds on pyranose rings. This is a characteristic peak typical of polysaccharide structures[27]. The 1076.80 cm^{-1} peak mainly represented C-O stretching in sugar ring backbones or symmetric stretching of C-O-C glycosidic bonds. This main peak reflects the characteristic properties of polysaccharides[28]. Additionally, the 828.00 cm^{-1} peak was a characteristic absorption of polysaccharides in the infrared spectrum[29].

3.3 Methylation analysis

Methylation analysis can elucidate the linkage patterns between monosaccharide residues within polysaccharides. It precisely localises linkage sites and delineates the substitution patterns of each

monosaccharide[30]. Analysis and quantification were performed via GC-MS. Retention durations were compared with those recorded in the literature and the CCRC database[31]. Tab. 1 illustrates the inferred linkage patterns. The gas chromatograms of the methylation analysis and the mass spectrometry data for PMAA are shown in Fig. S2A-B. The data suggest that Ahp-1 is a galactomannan. Four primary glycosidic bonds were identified: 6-Gal, 6-Glc, t-Fuc, and 2,6-Gal.

Tab. 1. Analysis of methylation results

Type of Linkage	Partially methylated alditol acetates	Retention time (min)	Mass fraction (m/z)	Molecular weight (Mw)	Relative molar ratio (%)
t-Ara(*p*)	1,5-di-*O*-acetyl-2,3,4-tri-*O*-methyl arabinitol	12.734	88,101,102,117,118,129,161	279	1.95
t-Fuc(*p*)	1,5-di-*O*-acetyl-6-deoxy-2,3,4-tri-*O*-methyl galactitol	13.598	72,89,102,115,118,131,162,175	293	10.26
t-Man(*p*)	1,5-di-*O*-acetyl-2,3,4,6-tetra-*O*-methyl mannitol	16.763	87,102,118,129,145,161,162,205	323	1.60
t-Gal(*p*)	1,5-di-*O*-acetyl-2,3,4,6-tetra-*O*-methyl galactitol	16.841	87,102,118,129,145,161,162,205	323	1.21
t-Glc(*p*)	1,5-di-*O*-acetyl-2,3,4,6-tetra-*O*-methyl glucitol	17.461	87,102,118,129,145,161,162,205	323	1.36
3-Gal(*p*)	1,3,5-tri-*O*-acetyl-2,4,6-tri-*O*-methyl galactitol	19.652	87,101,118,129,161,202,234	351	0.82
6-Glc(*p*)	1,5,6-tri-*O*-acetyl-2,3,4-tri-*O*-methyl glucitol	20.502	87,99,102,118,129,162,189,233	351	13.24
6-Gal(*p*)	1,5,6-tri-*O*-acetyl-2,3,4-tri-*O*-methyl galactitol	21.545	87,99,102,118,129,162,189,233	351	58.81
2,6-Gal(*p*)	1,2,5,6-tetra-*O*-acetyl-3,4-di-*O*-methyl galactitol	24.246	87,88,99,100,129,130,189,190	379	9.20
3,4,6-Glc(*p*)	1,3,4,5,6-penta-*O*-acetyl-2-*O*-methyl galactitol	25.027	97,118,129,139,160,333	407	1.54

We compared the structure and mechanism of action of the previously reported *A. heimuer* polysaccharide with Ahp-1. Relevant details are provided in supplementary Tab. S2-S3. This result differs from the polysaccharide structure and activity mechanism reported in prior studies, a discrepancy likely arising from variations in extraction methods and conditions[32-34]. Thus, we propose that Ahp-1 may represent a novel polysaccharide derived from *A. heimuer*. Additionally, this study found that Ahp-1 is rich in 6-Gal and 6-Glc bonds, exhibiting structural characteristics similar to those of the active polysaccharides reported in the literature from *Ziziphus jujuba*. According to literature reports, the active polysaccharides isolated from *Ziziphus jujuba* primarily contain glycosidic bonds with galactose and glucose residues. Its abundant galacturonic acid content enhances antioxidant bioactivity[35,36]. The t-Fuc residues and 2,6-Gal residues subsequently identified in Ahp-1 were confirmed to enhance antioxidant capacity and immunomodulatory effects[37]. In summary, we hypothesise that Ahp-1 may possess potent antioxidant activity.

3.4 Crystal characteristics and molecular surface morphology

We conducted experiments using AFM, Raman spectroscopy, and SEM to examine the molecular structural characteristics, micro-morphology, nanoscale architecture, surface morphology, and macroscopic aggregation state of Ahp-1.

Fig. 1G shows that AFM topography images reveal Ahp-1 has a significant gel-like network structure, indicating the sample's elevated viscosity and molecular aggregation at room temperature. In the AFM three-dimensional representation, Ahp-1 exhibits an average surface roughness (Ra) of 1.53 nm and a root-mean-square roughness (Rq) of 1.15 nm. The height difference between the edges and the chain centers indicates that the sample consists of dimers formed by the cross-linking of polysaccharide chains[38].

The Raman shift at 413 cm^{-1} corresponds to the vibrational peak of the pyran ring. The peak at 820 cm^{-1} is indicative of the C-C-O-C-O bond. The region 1050-1168 cm^{-1} displays distinctive C-O bond peaks. The region 1272-1345 cm^{-1} reveals recognizable C-O-H bond peaks[39]. A distinct peak at 2953 cm^{-1} corresponds to C-H stretching vibration. The wide raman peak between 3200-3600 cm^{-1} is associated with O-H stretching vibration (Fig. 1H).

SEM demonstrated that Ahp-1 mostly comprises lamellar structures that join to create a network, with strongly interlocked terminal connections (Fig. 1I).

3.5 Ahp-1 exerts a protective effect against APAP-induced acute liver injury

Initially, we investigated the hepatoprotective effect of Ahp-1 in mice with APAP-induced injury (Fig. 2A). Results demonstrated that compared with the APAP group, the Ahp-1 group exhibited significantly reduced hepatic parameters (Fig. 2B). Serum ALT and AST levels showed marked decreases (Fig. 2C). Inflammatory cell infiltration and vacuolation within hepatic lobules were ameliorated (Fig. 2D). Concurrently, it significantly enhanced the activity of SOD, GSH-Px, and CAT in serum and liver tissue while reducing MDA levels (Fig. 2E-F). ALT and AST levels in the APAP group exceeded the established safety range for KM mice, validating the model's efficacy (physiological safety range provided by Jiangsu Jingmei Biotechnology Co., Ltd.). Furthermore, through 21 days of oral administration of Ahp-1 solution, we observed no toxic effects. The mice exhibited sustained weight gain, and no significant alterations in transaminase activity were noted (Fig. S3A-B). Our findings demonstrate that Ahp-1 substantially alleviates APAP-induced DILI in mice, with the medium-dose cohort displaying the greatest efficacy. Consequently, this dosage was selected for further examinations.

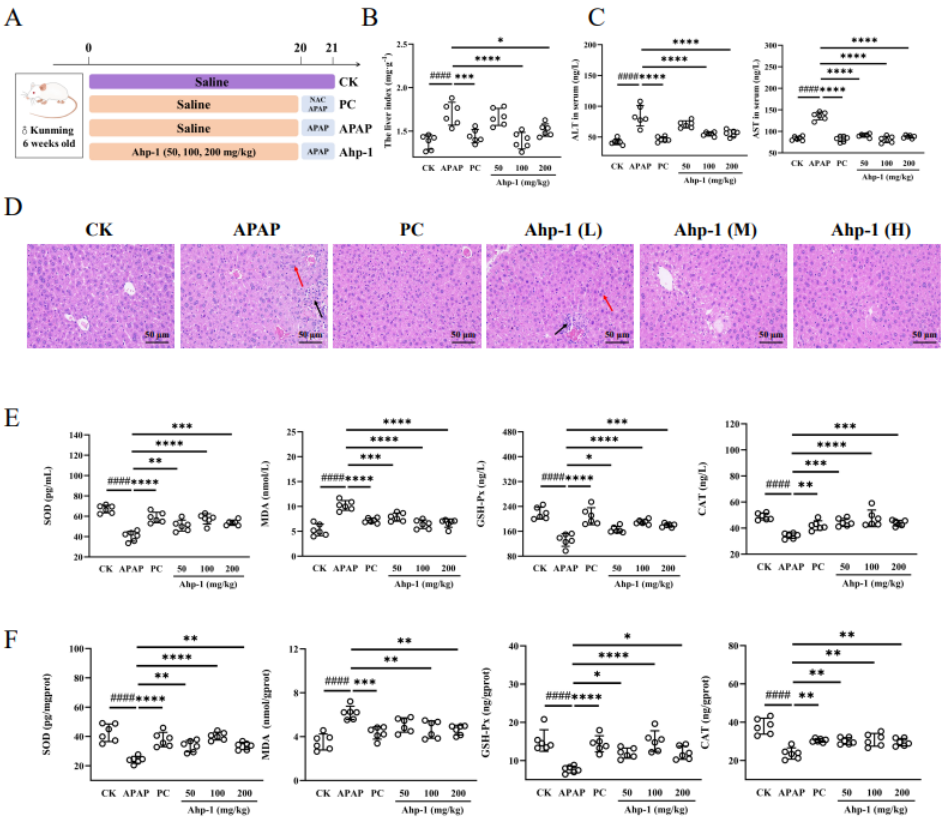

Fig. 2. Ahp-1 demonstrates a marked ameliorative effect on drug-induced liver injury (DILI). (A) Schematic of the experimental process. (B) Effect of Ahp-1 on liver indices in acetaminophen (APAP) mice (n = 6). (C) Serum ALT, AST indices in mice administered APAP, N-acetylcysteine (NAC), treatment with Ahp-1 (n = 6). (D) Liver H&E staining (n = 3). (E) Serum oxidation index in APAP mice treated with Ahp-1 (n = 6). (F) Liver tissue oxidation index in APAP mice treated with Ahp-1 (n = 6). Statistically significant differences are shown with asterisks as follows: $^{\#\#\#\#}P < 0.0001$; $^{*}P < 0.05$; $^{**}P < 0.01$; $^{***}P < 0.001$; $^{****}P < 0.0001$.

3.6 Ahp-1 exerts a beneficial effect on the gut microbiota of APAP mice

Research indicates that gut microbiota may exert a key regulatory role in improving DILI by modulating the body's oxidative stress balance[40]. Thus, we investigated the effects of Ahp-1 on the gut microbiota of APAP-treated mice. Fig. 3A demonstrates that Ahp-1 enriches dominant phylum-level species composition. Following Ahp-1 gavage, the mice's community structure converged towards that of the CK group (Fig. 3B). The increase in his alpha diversity index indicates enhanced microbial diversity within the gut (Fig. 3C). Furthermore, Ahp-1 intervention led to an increase in the number of OTUs, suggesting that Ahp-1 alleviated the disruption in species composition within the mouse gut (Fig. 3D).

We further investigated the differential changes in APAP-induced alterations to gut microbial genus abundance in mice. LEfSe analysis demonstrated that Ahp-1 supplementation elevated the abundances of *Roseburia* and *Dubosiella* (Fig. 3E). *Roseburia* is a key butyrate-producing genus implicated in regulating intestinal pathogenic processes[41]. *Dubosiella* synthesizes propionate and lysine to modulate colonic Treg/Th17 immune balance, thus alleviating colitis and improving mucosal barrier integrity[42]. Further analysis of gut microbial disparities among groups (Fig. 3F) revealed increased relative abundances of *Kineothrix*, *Muribaculum*, *Lactobacillus*, *Prevotella* and *Eubacterium* in the Ahp-1 group. *Kineothrix* is associated with hepatic health and mitigates murine steatohepatitis via lipid metabolism regulation[43].

Muribaculum and *Prevotella* metabolize dietary polysaccharides through various carbohydrate-degrading enzymes, maintaining intestinal mucus layer structure or function[44,45]. *Eubacterium* boosts intestinal epithelial tight junction function by producing butyrate, thereby protecting the intestinal mechanical barrier[46]. These findings indicate that Ahp-1 can enrich beneficial bacteria and regulate the relative abundance and diversity of the intestinal microbiota in APAP mice.

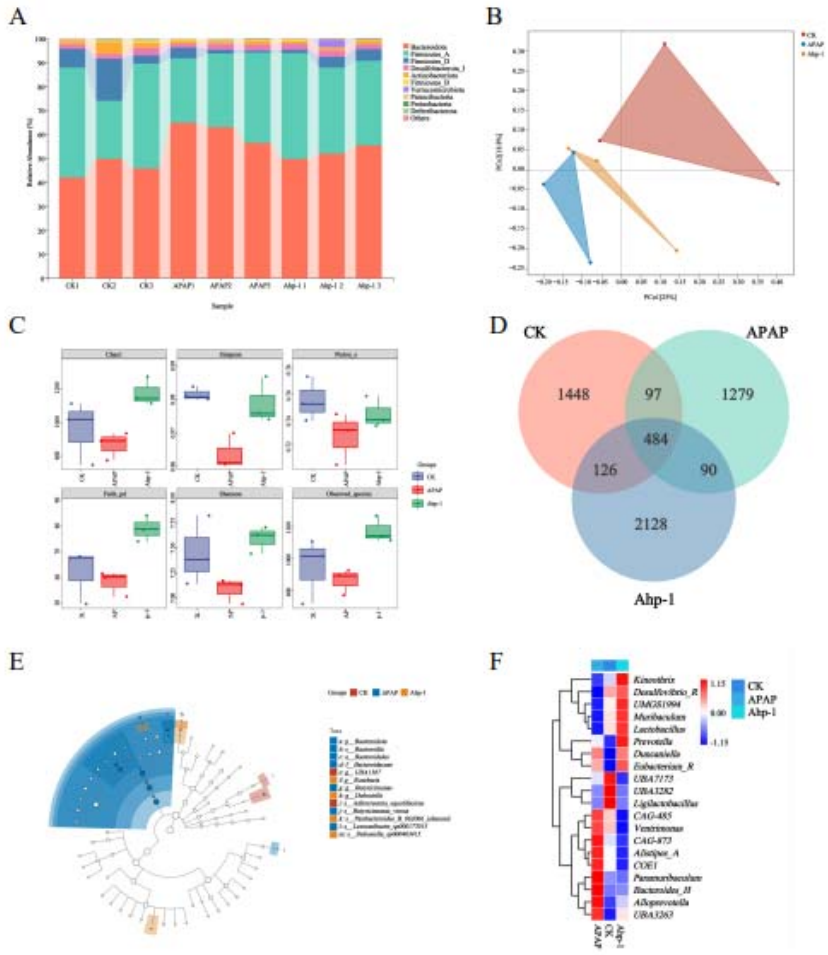

Fig. 3. Ahp-1 exerts a beneficial effect on the gut microbiota of APAP mice. (A) Species composition analysis (n = 3). (B) Principal component analysis clustering (n = 3). (C) Microbial diversity in the gut flora (n = 3). (D) Differential microbial community venn diagram (n = 3). (E) LefSe analyses of differential bacterial genera (n = 3). (F) Heat map of different groups of related genera (n = 3).

3.7 Ahp-1 can increase beneficial metabolites in APAP mice

Metabolites act as the crucial connection between gut microbiota and liver damage, with their dysregulation directly or indirectly facilitating the initiation and advancement of DILI[47]. Therefore, we used non-targeted metabolomics to examine the impact of Ahp-1 on metabolites in APAP-treated mice. The comparison of differential metabolites between the APAP and Ahp-1 groups identified 72 unique metabolites, consisting of 64 upregulated and 6 downregulated metabolites (Fig. 4A). The CK and APAP groups exhibited 196 significantly different metabolites, with 32 shared significantly different metabolites between the two groups (Fig. 4B). Correlation analysis results, as depicted in Fig. 4C, revealed positive correlations between Trigonelline and N-Acetylserotonin (NAS), Riboflavin, Gentisic acid, among others, in the Ahp-1 group

compared to the APAP group. Studies demonstrate that Trigonelline has anti-inflammatory and antioxidant characteristics[48]. Malvidin has protective benefits against lipopolysaccharide-induced acute liver damage in mice via regulating the Nrf2 and NLRP3 pathways[49]. NAS reduces serum AST levels and mitigates histological liver lesions[50]. Gentisic acid raises plasma liver enzyme levels and boosts hepatic antioxidant capacity via the modulation of the Nrf2 pathway[51].

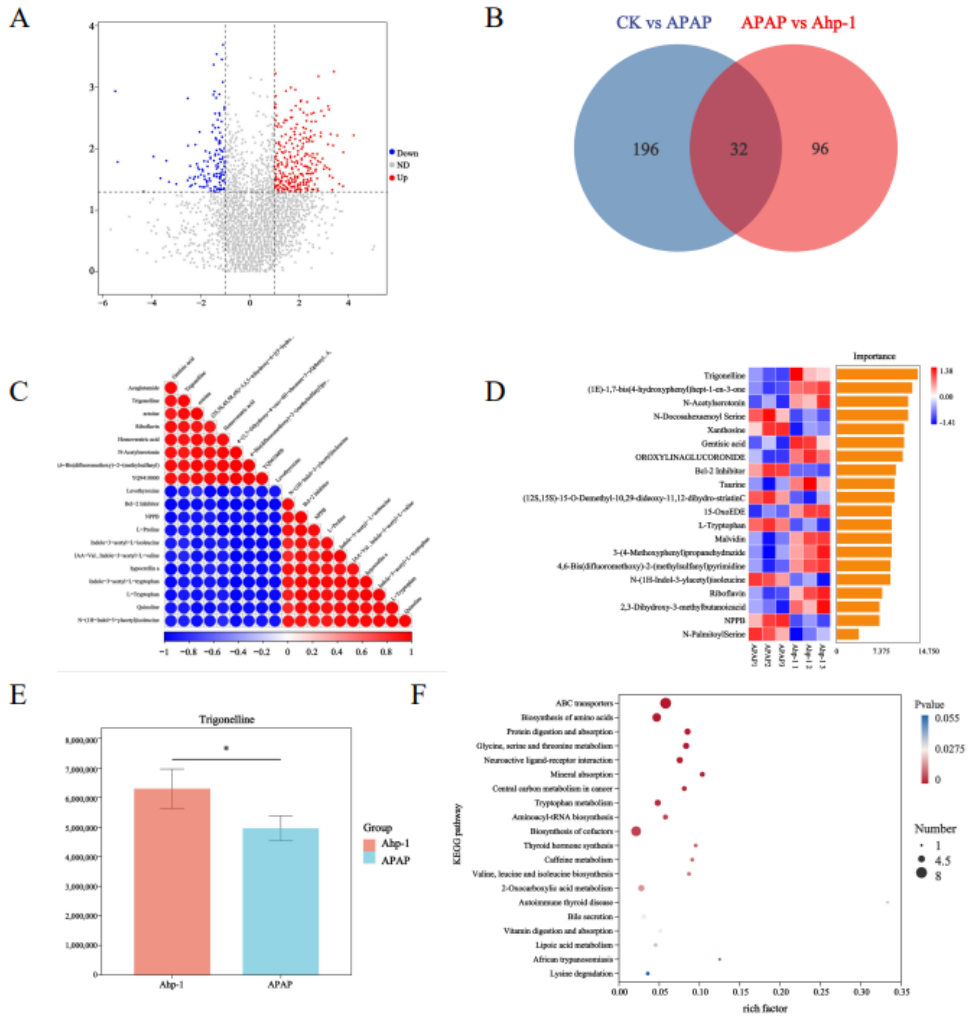

Fig. 4. Ahp-1 can increase beneficial metabolites in APAP mice. (A) Metabolite volcano plot (n = 3). (B) Number of differential metabolites (n = 3). (C) Metabolite correlation analysis (n = 3). (D) Metabolite importance ranking (n = 3). (E) Differential metabolite relative quantification (n = 3). (F) KEGG pathway prediction (n = 3). Statistically significant differences are shown with asterisks as follows: $^{*}P < 0.05$.

To further investigate differential metabolite changes, we ranked metabolites by significance. We identified Trigonelline as the metabolite exhibiting the most pronounced change between the Ahp-1 group and the APAP group (Fig. 4D). Trigonelline levels were significantly elevated in the Ahp-1 group (Fig. 4E). Furthermore, KEGG enrichment analysis revealed that the most enriched pathway for differential metabolites was ABC transporters (Fig. 4F). ABC transporters participate in the transmembrane transport of lipids, and lipid metabolism is closely associated with AMPK activity[52]. Moreover, it can reduce intracellular oxidative stress levels, thereby exerting feedback regulation on the Nrf2 signaling pathway to maintain homeostasis[53]. Based on the aforementioned findings, we hypothesize that Ahp-1 inhibits APAP-induced hepatotoxicity through its association with the ABC transporter metabolic pathway, potentially mediated via the AMPK and

Nrf2 signaling pathways.

3.8 Ahp-1 can ameliorate DILI by modulating intestinal flora

To elucidate the role of gut microbiota in Ahp-1's amelioration of DILI, this study employed FMT to verify whether gut microbiota can suppress the occurrence of DILI (Fig. 5A). Following antibiotic depletion, no DNA was detected in mouse feces. Microbial diversity indices and biomass decreased, confirming the successful establishment of the pseudo-germ-free mouse model (Fig. 5B, Fig. S4A-B). The Ahp-FMT group significantly reduced serum ALT and AST levels in APAP-treated mice (Fig. 5C). It alleviated hepatic inflammatory cell infiltration and oedematous vacuoles (Fig. 5D). It also markedly increased GSH-Px, SOD, and CAT activity in liver and serum, while decreasing MDA activity (Fig. 5E-F). However, in mice continuously cleared by ABX, Ahp-1 failed to alleviate elevated ALT and AST levels or hepatic lesions (Fig. 5G-I). Thus, our results validate that Ahp-1 provides hepatoprotective benefits via the gut microbiome.

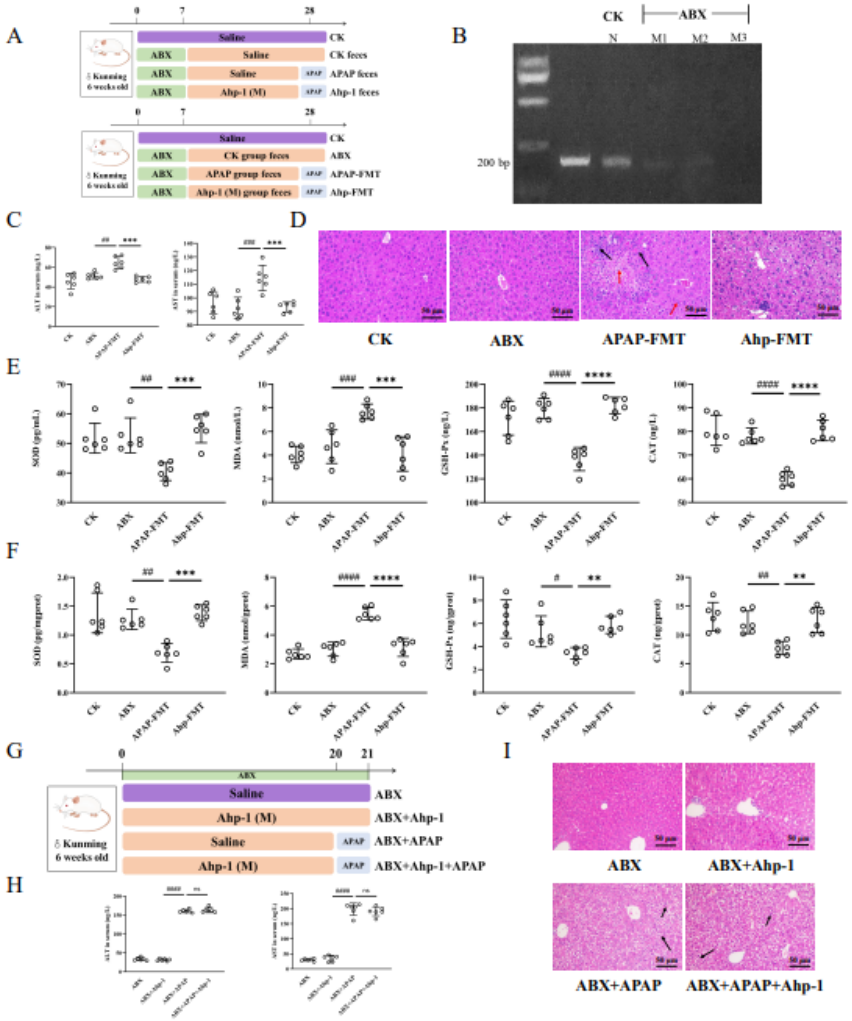

Fig. 5. Ahp-1 can ameliorate DILI by regulating intestinal flora. (A) Schematic of the experimental process. (B) Fecal DNA concentration (n = 3). (C) Serum ALT, AST indices in APAP mice after fecal microbiota transplantation (FMT) (n = 6). (D) Liver H&E staining (n = 3). (E) Serum oxidation index in APAP mice after FMT (n = 6). (F) Liver tissue oxidation index in APAP mice after FMT (n = 6). (G) Schematic of the experimental process. (H) ALT, AST biochemical indices in APAP mice after antibiotic clearance (n = 6). (I) Liver H&E staining (n = 3). Statistically significant differences are shown with asterisks as follows: $^{\#}P < 0.05$; $^{\#\#}P < 0.01$; $^{\#\#\#}P < 0.001$; $^{\#\#\#\#}P < 0.0001$; $^{**}P < 0.01$; $^{***}P < 0.001$; $^{****}P < 0.0001$; ns, no significant differences.

3.9 FMT can protect against intestinal barrier damage in APAP mice

The function of the intestinal barrier depends on the integrity of the mucosa. A reduction in the levels of tight junction proteins and mucins within the intestinal epithelium will lead to bacterial invasion, triggering various diseases[54]. Therefore, we assessed the effects of FMT on the expression of Occludin, Claudin-1, ZO-1, and Muc2 via immunofluorescence analysis. Fig. 6A demonstrates reduced fluorescence intensity for Occludin, Claudin-1, ZO-1, and Muc2 in the APAP-FMT group. The Ahp-FMT group exhibited a marked increase, with a clearly defined and intact fluorescence signal distribution.

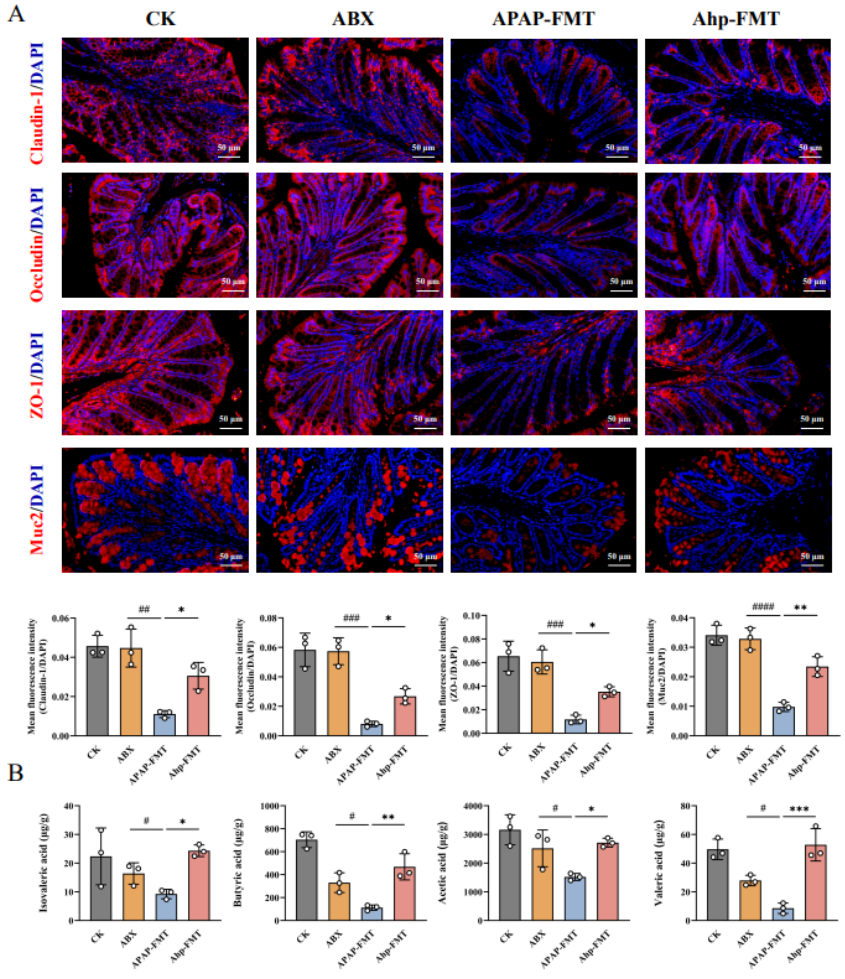

Fig. 6. FMT can protect against intestinal barrier damage in APAP mice. (A) Immunofluorescence expression levels of tight junction proteins and mucins in the intestinal barrier. (B) Short-chain fatty acid (SCFAs) content ($n = 3$). Statistically significant differences are shown with asterisks as follows: $^{\#}P < 0.05$; $^{\#\#}P < 0.01$; $^{\#\#\#}P < 0.001$; $^{\#\#\#\#}P < 0.0001$; $^{*}P < 0.05$; $^{**}P < 0.01$; $^{***}P < 0.001$.

SCFAs serving as the primary energy substrate for colonic cells, maintain intestinal barrier integrity, reduce intestinal permeability, and delay hepatic injury[55]. The quantitative examination of SCFAs indicated that the Ahp-FMT group had increased amounts of butyrate, valerate, acetate, and isovalerate (Fig. 6B). According to the literature, butyrate and valerate stimulate intestinal epithelial cell proliferation via activating the AMPK signaling system, hence expediting the healing of injured epithelium. They further access the liver via the portal vein, triggering the Nrf2 antioxidant pathway to indirectly alleviate hepatic damage[56]. Besides, acetate and isovalerate decrease gut pH, limiting pathogenic bacterial development and fostering probiotic

proliferation[57]. Our research indicates that FMT can modulate the intestinal barrier and elevate SCFA levels.

3.10 FMT can modulate the gut microbiota of APAP mice

To further elucidate changes in gut microbiota following FMT, we conducted microbial diversity analyses. At a sequencing depth of 20,000, the curve levelled off, indicating sufficient sampling depth (Fig. 7A). Ahp-FMT enriched microbial diversity in mouse intestines (Fig. 7B) and markedly improved gut microbiota composition (Fig. 7C-D). Within the Ahp-FMT group, relative abundances of *Alloprevotella*, *Mucispirillum*, and *Alistipes* decreased, while those of *Lachnospiraceae_NK4A136_group*, *Desulfovibrio*, *Lactobacillus*, *Parabacteroides*, and *Blautia* increased (Fig. 7E-F). *Lachnospiraceae* is a potentially beneficial taxon that metabolizes various carbohydrates to promote the synthesis of butyrate, acetate and other SCFAs[58]. *Blautia* lowers intestinal pH to inhibit pathogenic bacterial growth, supplies energy for intestinal epithelial cells, alleviates inflammation and improves intestinal barrier function[59]. *Lactobacillus* is a well-recognized gut probiotic that enhances intestinal immune function[60]. *Parabacteroides* is linked to lipid metabolism and transport, intestinal barrier repair and the amelioration of metabolic disorders[61]. Collectively, these findings confirm that FMT can modulate the species composition and relative abundance of the gut microbiota in APAP mice.

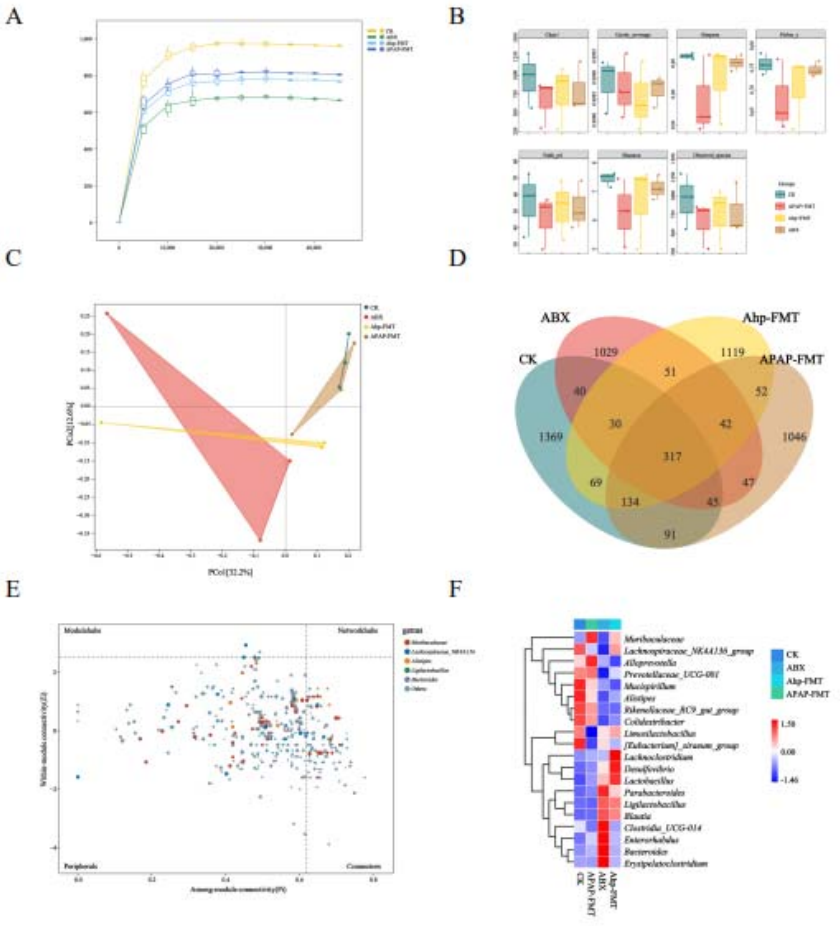

Fig. 7. FMT can modulate the gut microbiota of APAP mice. (A) Sequencing depth detection (n = 3). (B) Microbial diversity in the gut flora (n = 3). (C) Principal component analysis clustering (n = 3). (D) Differences in microbial abundance across groups (n = 3). (E) Abundance Difference Statistics (n = 3). (F) Heat map of different groups of related genera (n = 3).

3.11 FMT can enrich advantageous metabolites in APAP mice

To elucidate metabolic changes during FMT, we conducted non-targeted metabolomics analysis. All metabolites were statistically categorised by chemical classification. Organic acids and their derivatives exhibiting the highest proportion in both positive and negative ions, followed by lipids and lipoid molecules (Fig. 8A-B). 27 differential metabolites were identified between the APAP-FMT and Ahp-FMT groups (Fig. 8C). Compared to the APAP-FMT group, Trigonelline exhibited the most significant change in the Ahp-FMT group (Fig. 8D-E). KEGG enrichment analysis revealed that the most enriched pathway for differential metabolites was Metabolic pathways, followed by ABC transporters (Fig. 8F). Trigonelline has been reported to promote transporter expression via the AMPK signaling pathway, inhibit key enzymes of hepatic gluconeogenesis, and reduce lipid accumulation in liver tissue[62]. Furthermore, Trigonelline can reduce MDA accumulation via the Nrf2/HO-1 pathway, thereby protecting cells from oxidative damage[63]. Therefore, we conducted in vitro cell functional validation. In vitro cellular studies demonstrate that the metabolite Trigonelline enhances the survival rate of THLE-2 cells (Fig. S5A). It enhances antioxidant activity (Fig. S5B), and mitigates APAP-induced damage via the AMPK/GSK3β and Nrf2/HO-1 signaling pathways (Fig. S5C, Fig. S6). Therefore, we hypothesize that Ahp-FMT may mitigate DILI via the AMPK/GSK3β and Nrf2/HO-1 signaling pathways, based on investigations of gut microbiota and non-targeted metabolomics.

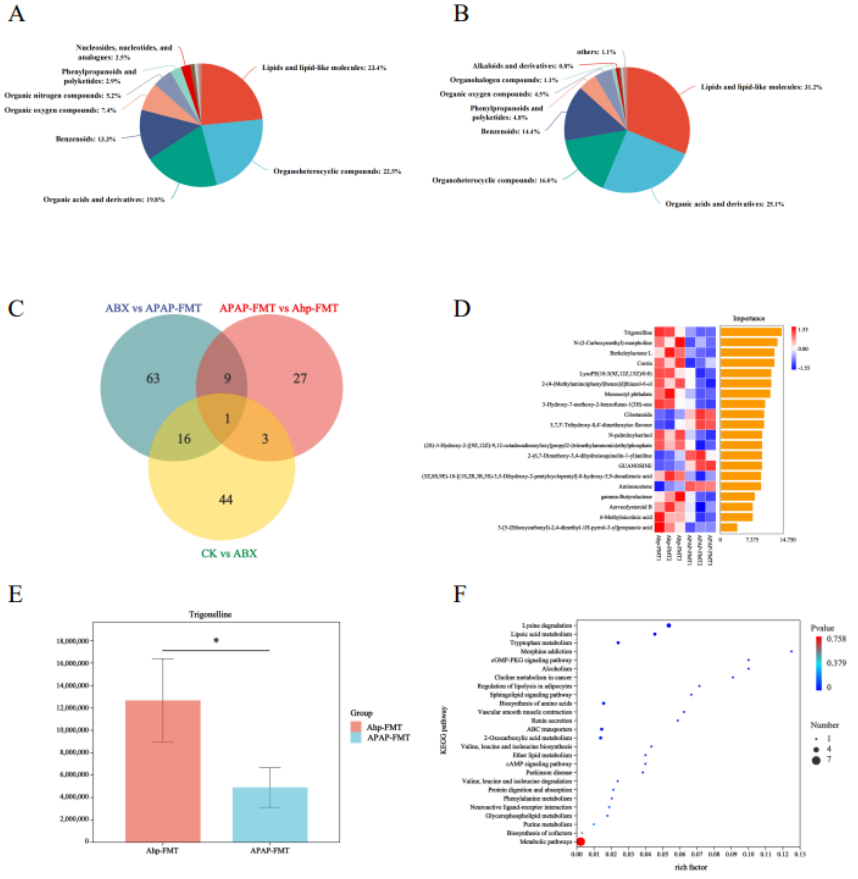

Fig. 8. FMT can enrich advantageous metabolites in APAP mice. (A) Percentage distribution of metabolites identified in positive ion mode across chemical classes (n = 3). (B) Proportion of metabolites identified in negative ion mode across chemical classes (n = 3). (C) Number of differential metabolites across different groups (n = 3). (D) Metabolite importance ranking (n = 3). (E) Differential metabolite relative quantification (n = 3). (F) KEGG pathway prediction (n = 3). Statistically significant differences are shown with asterisks as follows: $^{*}P < 0.05$.

3.12 Ahp-FMT ameliorates DILI via the AMPK/GSK3β and Nrf2/HO-1 signaling pathways

To further elucidate the mechanism by which Ahp-FMT ameliorates DILI, we conducted validation via western blot analysis. As depicted in Fig. 9A-C and Fig. S7, Ahp-FMT significantly elevated the phosphorylation levels of AMPK, AKT, and ACC, suppressed GSK3β expression, and activated the AMPK/GSK3β signaling pathway. It markedly elevated Nrf2 nuclear translocation and promoted the expression of NQO1, HO-1, GCLM, and GCLC, thereby protecting against APAP-induced hepatic injury. Additionally, we employed Compound C to inhibit expression in mice prior to intervention (Fig. 10A). Results demonstrated that following Compound C treatment, Ahp-1 and Ahp-FMT could no longer modulate the protein expression of AMPK/GSK3β and Nrf2/HO-1 (Fig. 10B, Fig. S8).

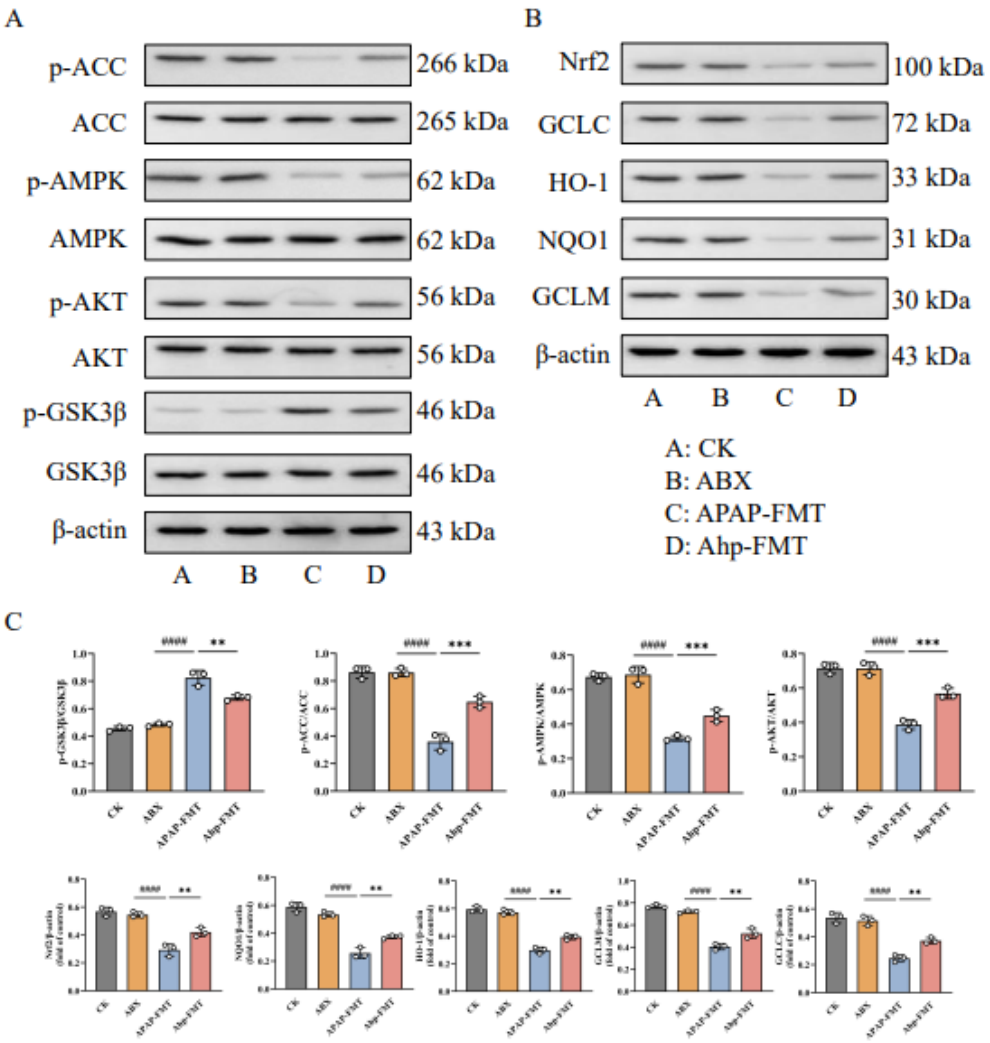

Fig. 9. FMT ameliorates APAP-induced acute liver injury by activating the AMPK/GSK3β and Nrf2/HO-1 signaling pathways. (A) AMPK/GSK3β pathway protein expression (n = 3). (B) Nrf2/HO-1 pathway protein expression (n = 3). (C) Quantitative analysis of signaling pathway proteins (n = 3). Statistically significant differences are shown with asterisks as follows: $^{\#\#\#\#}P < 0.0001$; $^{**}P < 0.01$; $^{***}P < 0.001$. Representative western blot images and quantitative analysis of protein expression from n = 3 independent biological replicates are shown.

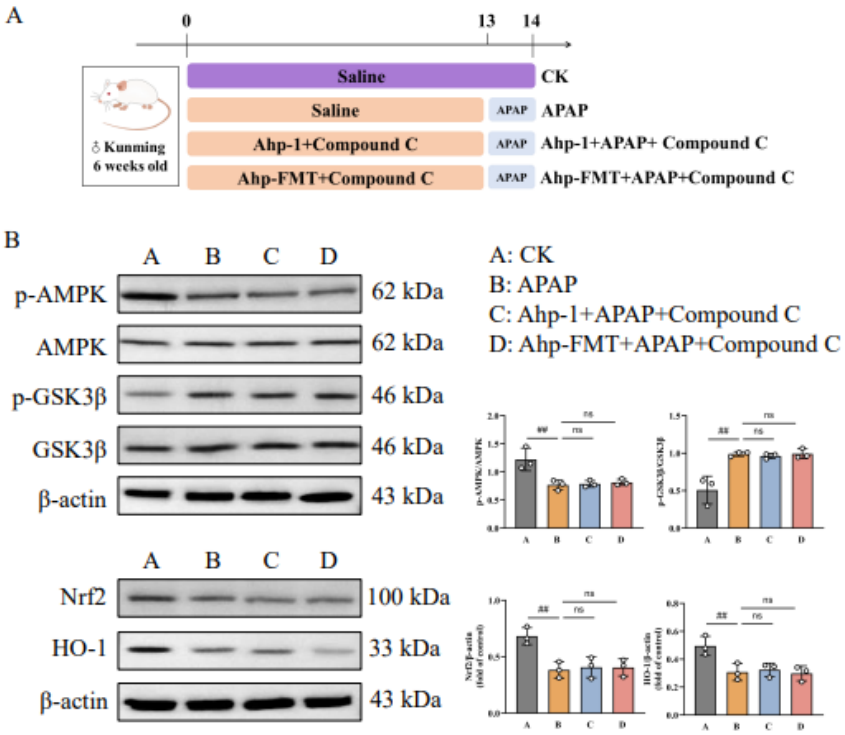

Fig. 10. Following the addition of antagonists, Abp-1 and Ahp-FMT failed to ameliorate DILI via the AMPK/GSK3β and Nrf2/HO-1 signaling pathways. (A) Schematic of the experimental process. (B) Protein expression levels and quantification of AMPK/GSK3β and Nrf2/HO-1 signaling pathways (n = 3). Statistically significant differences are shown with asterisks as follows: $^{\#\#}P < 0.01$; ns, no significant differences. Representative western blot images and quantitative analysis of protein expression from n = 3 independent biological replicates are shown.

Liver AMPK acts as a cellular energy sensor that regulates glucose and lipid metabolism, its activation modulates downstream glycolytic and lipid metabolic genes. It can also drive hepatic glycogen synthesis by upregulating glycogen synthase expression[64]. AMPK orchestrates cellular energy metabolism via downstream targets such as ACC, and enhances glycogenesis by upregulating GSK3β-an emerging regulator of Nrf2[65]. As a key transcription factor in the intracellular antioxidant defense system, Nrf2 maintains cellular redox homeostasis and protects against oxidative stress by regulating downstream antioxidant proteins (HO-1, NQO1)[66]. Additionally, GCLC and GCLM are rate-limiting enzymes in GSH synthesis, with their expression directly governing GSH production[67]. Based on these findings, we demonstrate that Ahp-FMT ameliorates APAP-induced acute liver injury by activating the AMPK/GSK3β and Nrf2/HO-1 signaling pathways.

4. Conclusion

This study presents the isolation of a novel polysaccharide (Ahp-1) from the fruiting bodies of *A. heimuer*, with a molecular weight of 270.161 kDa. The primary glycosidic connections are 6-Gal, 6-Glc, t-Fuc, and 2,6-Gal. Ahp-1 maintains gut microbial balance and associated metabolite levels in mice, increases SCFAs concentrations, and rehabilitates the intestinal mucosal barrier. Moreover, Ahp-1 confers a protective effect against APAP-induced liver damage via activating the AMPK/GSK3β and Nrf2/HO-1 signaling pathways and the gut microbiota, thereby alleviating oxidative stress. This study provides a theoretical foundation for the development of hepatoprotective pharmaceuticals or functional foods produced from *A. heimuer*

polysaccharides.

Acknowledgements

This work was supported by the National Key Research and Development Program of China (2021YFD1600401).

Ethics statement

All animal tests were performed in complete compliance with the regulations set out by the Laboratory Animal Welfare and Ethics Committee of Jilin Agricultural University, China (Approval no. 2024 08 08 001). Adheres to EU Directive 2010/63 concerning the protection of animals used for research purposes.

Data availability

16S rRNA sequencing and metabolomics data will be made available on request.

Conflict of Interest

The authors have declared no conflict of interest.

References

[1] H. Jaeschke, A. Ramachandran, Acetaminophen hepatotoxicity: paradigm for understanding mechanisms of drug-induced liver injury, Annu. Rev. Pathol. 19 (2024) 453-478. https://doi.org/10.1146/annurev-pathmechdis-051122-094016.

[2] M. Kotulkar, D. Paine-Cabrera, S. Abernathy, et al., Role of HNF_4alpha-cMyc interaction in liver regeneration and recovery after acetaminophen-induced acute liver injury, Hepatology. 78 (2023) 1106-1117. https://doi.org/10.1097/HEP.0000000000000367.

[3] K.P. Matchett, J.R. Wilson-Kanamori, J.R. Portman, et al., Multimodal decoding of human liver regeneration, Nature 630 (2024) 158-165. https://doi.org/ 10.1038/s41586-024-07376-2.

[4] S. Ali, J. Cervantes, Restoring gut microbial balance: the role of *Collinsella* in tuberculosis management, J. Invest. Med. (2025) 10815589251352523. https://doi. org/10.1177/10815589251352523.

[5] X. Lv, S. Li, Y. Yu, et al., Crustin defense against *Vibrio parahaemolyticus* infection by regulating intestinal microbial balance in *Litopenaeus vannamei*, Mar. Drugs 21 (2023). https://doi.org/10.3390/md21020130.

[6] F.T. Borsoi, I.A. Neri-Numa, W.Q. de Oliveira, et al., Dietary polyphenols and their relationship to the modulation of non-communicable chronic diseases and epigenetic mechanisms: a mini-review, Food Chem. 6 (2023) 100155. https://doi.org/10.1016/j.fochms.2022.100155.

[7] S.M. Jankovic, Acetaminophen toxicity and overdose: current understanding and future directions for NAC dosing regimens, Expert Opin. Drug Metab. Toxicol. 18 (2022) 745-753. https://doi.org/10.1080/17425255.2022.2151893.

[8] J. Kim, Y. Park, M. Jang, Identification of laccase family of *Auricularia auricula-judae* and structural prediction using alphafold, Int. J. Mol. Sci. 25 (2024). https://doi.org/10.3390/ijms252111784.

[9] S. Xu, Y. Zhang, K. Jiang, Antioxidant activity in vitro and in vivo of the polysaccharides from different varieties of *Auricularia auricula*, Food Funct. 7 (2016) 3868-3879. https://doi.org/10.1039/c6fo00686h.

[10] S. Nilkhet, K. Mongkolpobsin, C. Sillapachaiyaporn, et al., M1 macrophages polarized by crude polysaccharides isolated from *Auricularia polytricha* exhibit anti-tumor effect on human breast cancer cells, Sci. Rep. 14 (2024) 8179. https://doi.org/10.1038/s41598-024-58208-2.

[11] Y. Zhang, Y. Zeng, Y. Men, et al., Structural characterization and immunomodulatory activity of exopolysaccharides from submerged culture of *Auricularia auricula-judae*, Int. J. Biol. Macromol. 115 (2018) 978-984. https://doi.org/10.1016/j.ijbiomac.2018.04.145.

[12] T. Wang, Y. Liu, C. An, et al., *Auricularia auricula* polysaccharide alleviates cyclophosphamide-induced liver injury in mice involving remodeling of the gut bacteriome, mycobiome, and metabolome, Int. J. Biol. Macromol. 281 (2024) 136703. https://doi.org/10.1016/j.ijbiomac.2024.136703.

[13] Y. Lin, H. Chen, Y. Cao, et al., *Auricularia auricula* melanin protects against alcoholic liver injury and modulates intestinal microbiota composition in mice exposed to alcohol intake, Foods 10 (2021). https://doi.org/10.3390/foods 10102436.

[14] Y. Xie, X. Pan, X. Liang, et al., Research progress on structural characterization and bioactivities of *Poria cocos* and *Ganoderma* polysaccharides, Food & Medicine Homology 2 (2025) 9420040. https://doi.org/10.26599/fmh.2025. 9420040.

[15] W. Zheng, S. Lan, W. Zhang, et al., Polysaccharide structure evaluation of *Ganoderma lucidum* from different regions in China based on an innovative extraction strategy, Carbohydr. Polym. 335 (2024) 122079. https://doi.org /10.1016/j.carbpol.2024.122079.

[16] C. Bao, M. Liu, Y. Liu, et al., A structurally distinct arabinose-bridged arabinogalactan from *Lycium barbarum* as a TLR4-activating adjuvant for nanovaccine-based cancer immunotherapy, Carbohydr. Polym. (2025) 124618. https://doi.org/10.1016/j.carbpol.2025.124618.

[17] F. Tong, Y. Zhou, Y. Xu, et al., Supramolecular nanomedicines based on host-guest interactions of cyclodextrins, Exploration 3 (2023) 20210111. https://doi.org /10.1002/EXP.20210111.

[18] Y. Liu, H. Zhou, P. Pang, et al., *Tremella* polysaccharide microneedles loaded with magnetic dental pulp stem cell intracellular vesicles used for androgenic alopecia, Stem Cell Res. Ther. 16 (2025) 161. https://doi.org/10.1186/s13287-025-04219-3.

[19] G. Fu, Y. Li, Y. He, et al., Extraction, structure and bioactivity of *Tremella fuciformis* polysaccharides: a review, Food & Medicine Homology (2025). https://doi.org/10.26599/fmh.2025.9420038.

[20] P. Ma, W. Sun, C. Sun, et al., Using gut microbiota and non-targeted metabolomics techniques to study the effect of xylitol on alleviating DSS-induced inflammatory bowel disease in mice, BMC Immunol. 26 (2025) 18. https://doi.org/ 10.1186/s12865-025-00700-z.

[21] M. Liu, C. Bao, X. Liang, et al., Specific molecular weight of *Lycium barbarum* polysaccharide for robust breast cancer regression by repolarizing tumor-associated macrophages, Int. J. Biol. Macromol. 261 (2024) 129674. https://doi.org/10.1016/j.ijbiomac.2024.129674.

[22] H. Lv, L. Hong, Y. Tian, et al., Corilagin alleviates acetaminophen-induced hepatotoxicity via enhancing the AMPK/GSK3β-Nrf2 signaling pathway, Cell Commun. Signal. 17 (2019) 2. https://doi.org/10.1186/s12964-018-0314-2.

[23] D. Saribal, H. Calis, Z. Ceylan, et al., Investigation of the structural changes in the hippocampus and prefrontal cortex using FTIR spectroscopy in sleep deprived mice, Spectroc. Acta Pt. A-Molec. Biomolec. Spectr. 321 (2024) 124702. https://doi.org/10.1016/j.saa.2024.124702.

[24] I. Serra, D. Piccinini, A. Paradisi, et al., Activity and substrate specificity of lytic polysaccharide monooxygenases: an ATR FTIR-based sensitive assay tested on a novel species from *Pseudomonas putida*, Protein. Sci. 31 (2022) 591-601. https://doi.org/10.1002/pro.4255.

[25] R. Bikmurzin, R. Bandzeviciute, A. Marsalka, et al., FT-IR method limitations for β-glucan analysis, Molecules 27 (2022). https://doi.org/10.3390/molecules 27144616.

[26] K. Przybyl, K. Koszela, F. Adamski, et al., Deep and machine learning using SEM, FTIR, and texture analysis to detect polysaccharide in raspberry powders, Sensors 21 (2021). https://doi.org/10.3390/s21175823.

[27] C. Sandt, J. Waeytens, A. Deniset-Besseau, et al., Use and misuse of FTIR spectroscopy for studying the bio-oxidation of plastics, Spectroc. Acta Pt. A-Molec. Biomolec. Spectr. 258 (2021) 119841. https://doi.org/10.1016/j.saa. 2021.119841.

[28] A. Nawrocka, M. Krekora, Z. Niewiadomski, et al., FTIR studies of gluten matrix dehydration after fibre polysaccharide addition, Food Chem. 252 (2018) 198-206. https://doi.org/10.1016/j.foodchem.2018.01.110.

[29] H. Kandori, Y. Mizutani, FTIR and raman spectroscopy of rhodopsins, Methods Mol Biol 2501 (2022) 207-228. https://doi.org/10.1007/978-1-0716-2329-9_10.

[30] C.W. LaFlamme, C. Rastin, S. Sengupta, et al., Diagnostic utility of DNA methylation analysis in genetically unsolved pediatric epilepsies and CHD_2 episignature refinement, Nat. Commun. 15 (2024) 6524. https://doi.org/10.1038/ s41467-024-50159-6.

[31] D. Huang, W. Shang, M. Xu, et al., Genome-wide methylation analysis reveals a $KCNK_3$-prominent causal cascade on

hypertension, Circ. Res. 135 (2024) e76-e93. https://doi.org/10.1161/CIRCRESAHA.124.324455.

[32] J. Liang, Z. Rao, S. Jiang, et al., Structure of an unprecedent glucuronoxylogalactoglucomannan from fruit bodies of *Auricularia auricula-judae* (black woody ear), Carbohydr. Polym. 315 (2023) 120968. https://doi.org /10.1016/j.carbpol.2023.120968.

[33] J. Tang, Z. He, B. Zhang, et al., Structural properties, bioactivities, structure-activity relationships and bio-applications of polysaccharides from *Auricularia auricula*: a review, Int. J. Biol. Macromol. 280 (2024) 135941. https://doi.org/ 10.1016/j.ijbiomac.2024.135941.

[34] Z. Yang, Y. Hu, J. Wu, et al., High-efficiency production of *Auricularia polytricha* polysaccharides through yellow slurry water fermentation and its structure and antioxidant properties, Front. Microbiol. 13 (2022) 811275. https://doi.org/ 10.3389/fmicb.2022.811275.

[35] X. Ji, Y. Yan, C. Hou, et al., Structural characterization of a galacturonic acid-rich polysaccharide from *Ziziphus Jujuba cv. Muzao*, Int. J. Biol. Macromol. 147 (2020) 844-852. https://doi.org/10.1016/j.ijbiomac.2019.09.244.

[36] X. Ji, C. Hou, Y. Yan, et al., Comparison of structural characterization and antioxidant activity of polysaccharides from jujube (*Ziziphus jujuba* mill.) Fruit, Int. J. Biol. Macromol. 149 (2020) 1008-1018. https://doi.org/10.1016/j.ijbiomac. 2020.02.018.

[37] Y. Li, X. Guo, R. Zhong, et al., Structure characterization and biological activities evaluation of two hetero-polysaccharides from *Lepista nuda*: cell antioxidant, anticancer and immune-modulatory activities, Int. J. Biol. Macromol. 244 (2023) 125204. https://doi.org/10.1016/j.ijbiomac.2023.125204.

[38] T. Zhang, M. Chen, D. Li, et al., Review of the recent advances in polysaccharides from *Ficus carica*: extraction, purification, structural characteristics, bioactivities and potential applications, Int. J. Biol. Macromol. 281 (2024) 136430. https://doi.org/10.1016/j.ijbiomac.2024.136430.

[39] X. Mo, D. Guo, Y. Jiang, et al., Isolation, structures and bioactivities of the polysaccharides from *Radix hedysari*: a review, Int. J. Biol. Macromol. 199 (2022) 212-222. https://doi.org/10.1016/j.ijbiomac.2021.12.095.

[40] T. Kovacs, B. Rauch, E. Miko, et al., Methods to assess the role of PARPs in regulating mitochondrial oxidative function, Methods Mol Biol 2609 (2023) 227-249. https://doi.org/10.1007/978-1-0716-2891-114.

[41] Y. Jiang, Z. Huang, W. Sun, et al., *Roseburia intestinalis*-derived butyrate alleviates neuropathic pain, Cell Host Microbe 33 (2025) 104-118. https:// doi.org/10.1016/j.chom.2024.11.013.

[42] T. Liu, M. Chen, C. Zhang, et al., Hypertension inhibition by *Dubosiella newyorkensis* via reducing pentosidine synthesis, npj Biofilms Microbomes 11 (2025) 34. https://doi.org/10.1038/s41522-025-00645-6.

[43] W. Guo, W. Qiu, J. Zhu, et al., The complete genome sequence of *Kineothrix* sp. MB12-c1, isolated from the feces of black soldier fly larvae, Microbiol. Resour. Announc. 13 (2024) e0100523. https://doi.org/10.1128/mra.01005-23.

[44] C. Chen, J. Wang, M. Cheng, et al., *Muribaculum intestinale*-derived 3-hydroxybutyric acid from heterophyllin B attenuated pulmonary fibrosis through IDO1-mediated ferroptosis, Pharmacol. Res. 212 (2025) 107587. https://doi.org /10.1016/j.phrs.2025.107587.

[45] D.C. Nieman, C.A. Sakaguchi, J.C. Williams, et al., Gut *Prevotella copri* abundance linked to elevated post-exercise inflammation, J. Sport Health Sci. 14 (2025) 101039. https://doi.org/10.1016/j.jshs.2025.101039.

[46] X. Liu, R. Wu, Y. Fan, et al., From gut to joint: the protective impact of *Eubacterium rectale* on rheumatoid arthritis, Front. Immunol. 16 (2025) 1607804. https://doi.org/10.3389/fimmu.2025.1607804.

[47] A. Winiarska-Mieczan, K. Jachimowicz-Rogowska, M. Kwiecien, et al., Regular consumption of green tea as an element of diet therapy in drug-induced liver injury (DILI), Nutrients 16 (2024). https://doi.org/10.3390/nu16172837.

[48] M. Membrez, E. Migliavacca, S. Christen, et al., Trigonelline is an NAD(+) precursor that improves muscle function during ageing and is reduced in human sarcopenia, Nat. Metab. 6 (2024) 433-447. https://doi.org/10.1038/s42255-024-00997-x.

[49] X. Mao, X. Liu, C. Wei, et al., Malvidin alleviates lipopolysaccharide-induced acute lung injury by modulating JAK2/STAT3 signaling to inhibit macrophage m1 polarization and oxidative stress, J. Agric. Food. Chem. 73 (2025) 13488-13501. https://doi.org/10.1021/acs.jafc.5c00077.

[50] F. Fang, J. Tang, J. Geng, et al., N-acetylserotonin derivative ameliorates hypoxic-ischemic brain damage by promoting PINK1/parkin-dependent mitophagy to inhibit NLRP3 inflammasome-induced pyroptosis, Int. Immunopharmacol. 153 (2025) 114469. https://doi.org/10.1016/j.intimp.2025.114469.

[51] I.A. Abdelmawgood, M.A. Kotb, H.S. Hassan, et al., Gentisic acid attenuates ovalbumin-induced airway inflammation,

oxidative stress, and ferroptosis through the modulation of Nrf2/HO-1 and NF-κb signaling pathways, Int. Immunopharmacol. 146 (2025) 113764. https://doi.org/10.1016/j.intimp.2024. 113764.

[52] H. Yang, T. Wang, C. Qian, et al., Gut microbial-derived phenylacetylglutamine accelerates host cellular senescence, Nat Aging 5 (2025) 401-418. https:// doi.org/10.1038/s43587-024-00795-w.

[53] A. Hengist, R.G. Davies, J. Walhin, et al., Ketogenic diet but not free-sugar restriction alters glucose tolerance, lipid metabolism, peripheral tissue phenotype, and gut microbiome: RCT, Cell Rep. Med. 5 (2024) 101667. https://doi.org /10.1016/j.xcrm.2024.101667.

[54] Y. Chen, S. Lin, L. Wang, et al., Reinforcement of the intestinal mucosal barrier via mucus-penetrating PEGylated bacteria, Nat. Biomed. Eng. 8 (2024) 823-841. https://doi.org/10.1038/s41551-024-01224-4.

[55] N. Li, L. Niu, Y. Liu, et al., Taking SCFAs produced by *Lactobacillus reuteri* orally reshapes gut microbiota and elicits antitumor responses, J. Nanobiotechnology 22 (2024) 241. https://doi.org/10.1186/s12951-024-02506-4.

[56] L. She, J. Sun, L. Xiong, et al., Ginsenoside RK1 improves cognitive impairments and pathological changes in alzheimer's disease via stimulation of the AMPK/Nrf2 signaling pathway, Phytomedicine 122 (2024) 155168. https://doi. org/10.1016/j.phymed.2023.155168.

[57] H. Ma, C. Xing, H. Wei, et al., Berberine attenuates neuronal ferroptosis via the AMPK-NRF2-HO-1-signaling pathway in spinal cord-injured rats, Int. Immunopharmacol. 142 (2024) 113227. https://doi.org/10.1016/j.intimp.2024. 113227.

[58] S. Deng, H. Cao, T. Li, et al., *Lachnospiraceae-bacterium* alleviates ischemia-reperfusion injury in steatotic donor liver by inhibiting ferroptosis via the $Foxo_3$-$Alox_{15}$ signaling pathway, Gut Microbes 17 (2025) 2460543. https://doi.org/ 10.1080/19490976.2025.2460543.

[59] J. Liu, X. Lv, T. Ye, et al., Microbiota-microglia crosstalk between *Blautia producta* and neuroinflammation of parkinson's disease: a bench-to-bedside translational approach, Brain. Behav. Immun. 117 (2024) 270-282. https://doi.org/ 10.1016/j.bbi.2024.01.010.

[60] S. Yue, Q. He, J. Picimbon, *Lactobacillus* for ribosome peptide editing cancer, Clin. Transl. Oncol. 25 (2023) 1522-1544. https://doi.org/10.1007/s12094-022-03066-5.

[61] T. Li, N. Ding, H. Guo, et al., A gut microbiota-bile acid axis promotes intestinal homeostasis upon aspirin-mediated damage, Cell Host Microbe 32 (2024) 191-208. https://doi.org/10.1016/j.chom.2023.12.015.

[62] Q. Zhao, B. Zhang, X. Wang, et al., Canagliflozin delays aortic valve calcification by enhancing the AMPK/Nrf2/HO-1 antioxidant signaling pathway in valvular interstitial cells, FASEB. J. 39 (2025) e70630. https://doi.org/10.1096/fj.20240 3109R.

[63] Y. Han, X. Wang, D. Yu, Roflumilast inhibits neuronal ferroptosis via AMPK/Nrf2/HO-1 signaling and promotes motor function recovery after spinal cord injury in rats, Cell. Signal. 134 (2025) 111930. https://doi.org/10.1016/j. cellsig.2025.111930.

[64] Z. Zhu, J. Sui, H. Cai, et al., *Lycium barbarum* polysaccharide regulates serum metabolites in type 2 diabetic patients with the metabolomics-based approach of GC-TOF-MS, Journal of Future Foods (2025). https://doi.org/10.1016/j.jfutfo. 2024.12.001.

[65] M.M. Ghazaly, G.E. Lee, N.L. Ma, et al., A review and a bibliometric analysis of tropical herbs and their bioactive compounds for modulating gut microbiota function and glucose regulation in type 2 diabetes, Food & Medicine Homology (2024). https://doi.org/10.26599/fmh.2025.9420068.

[66] Y. Liu, Y. Cheng, N. Xiang, et al., Aerobic exercise improves BK_{Ca} channel-mediated vasodilation in diabetic vascular smooth muscle via AMPK/Nrf2/HO-1 pathway, Acta Diabetol. 61 (2024) 425-434. https://doi.org/10.1007/s00592-023-02210-z.

[67] X. Bai, Y. Zhu, J. Jie, et al., Maackiain protects against sepsis via activating AMPK/Nrf2/HO-1 pathway, Int. Immunopharmacol. 108 (2022) 108710. https://doi.org/10.1016/j.intimp.2022.108710.